

doi:10.3969/j.issn.1001-4616.2019.04.019

Fractal Dimension Features from Catchment Boundary Profile(CBP) of Small Watersheds in the Northern Shaanxi Province of China

Kamila Kabo-bah^{1,2,3}, Tang Guoan^{1,4}, Yang Xin^{1,5}, Na Jiaming⁴, Xiong Liyang⁵

(1.School of Geography, Nanjing Normal University, Nanjing 210023, China)

(2.School of Geosciences, University of Energy and Natural Resources, Sunyani 214, Ghana)

(3.Earth Observation Research and Innovation Centre (EORIC), University of Energy and Natural Resources, Sunyani 214, Ghana)

(4.Key Laboratory of Virtual Geographic Environment(Nanjing Normal University), Ministry of Education, Nanjing 210023, China)

(5.Jiangsu Center for Collaborative Innovation in Geographical Information Resource Development and Application, Nanjing 210023, China)

Abstract: The Loess Plateau of the Northern Shaanxi Province continues to be an important geomorphological research zone as a result of its history and geology evolution. This paper assessed the fractal properties of Catchment Boundary Profiles(CBP) generated from a 30 m ASTER Digital Elevation Model(DEM) for the study area. Three fractal models were applied; Box Counting, Higuchi and Hurst. The methods showed slight variation of fractal dimension's(FD) estimates for each CBP, with close estimates between the Box Counting and Higuchi models. The Box counting method was the most consistent and accurate while the Higuchi overestimated in some cases. The FD results shows close similarity with CBP complexity and harmonic behaviour, revealing the fractals sensitivity to changes in geomorphological characteristics irrespective of the size of the object under investigation. The results also closely relate to previous works landform classification and dynamic analysis using other methods. The findings from this research would provide vital information for future land use planning purposes in the region and complement other research interested in the application of fractals for modelling on climate related studies.

Key words: box counting, Higuchi, Hurst, digital elevation model(DEM), fractal dimension

CLC number: P208 **Document code:** A **Article ID:** 1001-4616(2019)04-0131-14

基于流域边界剖面线的陕北小流域分形特征

卡米拉^{1,2,3}, 汤国安^{1,4}, 杨 昕^{1,5}, 那嘉明⁴, 熊礼阳⁵

(1.南京师范大学地理科学学院, 江苏 南京 210023)

(2.能源与自然资源大学地球科学学院, 加纳 苏尼亚尼 214)

(3.能源与自然资源大学地球观测研究和创新中心, 加纳 苏尼亚尼 214)

(4.南京师范大学虚拟地理环境教育部重点实验室, 江苏 南京 210023)

(5.江苏省地理信息资源开发与利用协同创新中心, 江苏 南京 210023)

[摘要] 陕北黄土高原因其独特的地貌特征而成为重要的地貌研究区域. 本文基于先进星载热辐射和反射辐射计(ASTER) 30 m 空间分辨率的数字高程模型(DEM) 数据提取的流域边界剖面线(CBP), 评价了陕北黄土高原小流域的分形特征. 通过对比盒计数法(BCM)、Higuchi 法(HIG) 和 Hurst 法(HUR) 3 个分形维数估算模型发现, 分维值计算结果略有不同. 其中, BMC 和 HIG 法计算结果更为接近. 当 HIG 法在某些地方的分维数估值过高时, 盒计数法表现出更好的一致性和稳定性, 适合于陕北黄土高原的分维值估算. 研究发现分维值的大小与流域边界剖面线的复杂程度和谐波效应紧密相关, 说明分维值对地貌特征变化敏感性与观测尺度无关. 本文得到的陕北地貌分形特征与前人通过其他方法得到的结果一致, 进一步证明了流域边界剖面线在地貌特征分析中的意义. 该结果有望为区域土地利用规划、应用分形特征进行气候相关研究建模提供参考.

[关键词] 盒计数法, Higuchi 法, Hurst 法, 数字高程模型(DEM), 分维数

Received data: 2019-03-29.

Foundation item: Supported by the National Natural Science Foundation of China(41771415, 41930102), the Priority Academic Program Development of Jiangsu Higher Education Institutions(164320H116).

Corresponding author: Yang Xin, professor, majored in digital terrain analysis. E-mail: xxinyang@njnu.edu.cn

Geomorphological research in the Loess Plateau has been targeted on the spatial phenomenon and the evolution of processes of the landforms^[1]. Various studies emanating from the understanding the varying changes in underlying geomorphology, changing climatic conditions to processes involved in soil and sediment formation and deposits have been conducted in the Loess Plateau^[2-5]. Other studies have used Digital Elevation Models (DEMs) to characterize hydrologic and landforms features in the Loess Plateau of China^[6-9].

For instance, reference can be made to the various research on the erosion and soil loess using different techniques based on the terrain characteristics in the study area^[10-12]. The use of DEMs have proven to provide valuable resource for extracting several possible geomorphologic features for characterizing and classifying landform-types. For example, Zhou et al^[13] used Positive-Negative(P-N) terrains based on DEMs to characterize the different landforms in the Loess Plateau of Northern Shaanxi Province. These studies complement and demonstrate the emerging importance of the use of DEMs to characterise landform complexity. Therefore, DEMs have provided an easy entry-point for landform characterising to obtain several features to describe their processes, evolution and phenomenon propagating landform dynamics and changes. Most studies rely on DEMs derived from topographic maps or from satellite imagery such as Shuttle Radar Topographic Mission (SRTM) or Advanced Space-borne Thermal Emission and Reflection Radiometer (ASTER). Depending the specific landform complexity in-depth study's needs, a higher or coarser resolution may be required. Generally, to examine the differential landform complexities, the use of high resolution DEMs is eminent.

However, traditional methods capture landform complexities and terrain roughness using DEM is not always able to reveal the various complexities including the anthropogenic effects. Fractal models have proven to be the best models to represent this phenomena. Fractal dimension is concise, and interpretative entity taking into consideration the physical information with respect to geophysical and geometrical characterisation of a natural terrain surface^[14]. For example, geologists use fractal dimension to model the natural surface roughness; as this is independent of the size of the observed surface^[15]. The reality is that, traditional problems of classical roughness descriptors such as standard deviation height and correlation length depends on the observation scale and the extension of the surface to which they are estimated^[14].

The application of fractal concepts in the remote-sensing micro-environment is a long-standing topic, confirmed and testified by applications regarding image analysis^[16], and, in particular, Catchment Boundary Profile (CBP)^[15]. Li et al^[17] examined the CBP of watersheds using DEM in the Loess Plateau of the Northern Shaanxi Province with some estimates on fractal dimension. The CBP were created from DEMs. The study focused on the extraction of the CBP, their statistical properties and using this parameter as a means of classifying the different landform complexity. However, the relationships between the Fractal Dimension properties and the Catchment Boundary Profile(CBP) properties were not been explored. Therefore, this study examined the CBPs derived from various watersheds using Advanced Spaceborne Thermal Emission and Reflection Radiometer (ASTER) 30 m DEM for the Northern Shaanxi Province. The study applied three fractal models for the estimation of the fractal dimension. The findings from this research is anticipated to support climate related studies on geomorphology and land use planning.

1 Materials and Methods

1.1 Study area

The study area is located between 107°28'E-111°15'E and 35°20'N-39°34'N showing the middle belt of the Loess Plateau. The Loess Plateau located in the North is characterised by North Mountains, an important part of the Loess Plateau in China(Fig. 1). The elevation ranges high in the North West but low in the south east. This part is usually covered by loess layer of 50-100 m in thickness, and maximum thickness up to 200 m.

The Shaanxi region is characterised by continental monsoon climate but shows distinctive regional differences. It is covered by mountainous areas with sloping fields. The average annual precipitation is 570 mm

falling within July–October. The average annual temperature is 13.8 °C and wind speed 1.7 m/s. The humid area aridity is less than 1.0, and semi-humid area has aridity in the range of 1.5 and 2.0. The climate in the region is characterised by warm, windy spring when the temperatures rise fast and become unsteady. The main rainfall is concentrated in the periods in July–September. According to report from Wang et al^[18], the average annual surface runoff is 42.58 billion m³ for many years, the quantity of water resources 44.5 billion m³ (i.e. ranking the 19th in China). The same report also indicates that the average per capita water resources stand at 1 280 m³, groundwater resources about 33.6 billion m³ and average evaporation losses estimates between 1 000–2 000 mm annually.

1.2 Dataset description

The Advanced Spaceborne Thermal Emission and Reflection Radiometer (ASTER) Digital Elevation Model (hereby referred to as GDEM2) was obtained from the Earth Explorer^[19]. The ASTER on NASA's Terra spacecraft collects in-track stereo using nadir- and aft looking near infrared cameras. Since 2000, these stereo pairs have been used to produce single-scene (60×60 km) digital elevation models having vertical accuracies generally between 10 m and 25 m in root-mean-square-error. The GDEM2 was validated using a comparison of the GDEM2 against the absolute geodetic references over the Conterminous US (CONUS), against the national elevation grids over Japan and US, against the Shuttle Radar Topography Mission (SRTM) 1 arc-second elevation grids over the US and 20 sites globally and against the space borne laser altimeter data present globally. The absolute vertical accuracy for the GDEM2 was found to be within −0.20 meters on average when compared against 18 000 geodetic control points over the CONUS, with an accuracy of 17 meters at the 95% confidence level^[20]. The Japan study found that the GDEM2 varied from the 10-meter national elevation grid by −0.7 m over bare areas and by 7.4 m over forested areas. The global altimeter research found that the GDEM2 was within 3 meters of the altimeter-derived control and also indicated sensitivity to the tree canopy height. The DEM downloaded for the study area has the highest elevation as 2 467 m and minimum elevation as 333 m. The mean elevation is 1 207 with standard deviation of 243.7 m with maximum slope and aspect being 89.6° and 360° respectively.

1.3 Catchment boundary profile (CBP) derivation

The sub-watersheds created in previous section were evaluated for their fractal dimension based on the Catchment Boundary Profile (CBP) Lines. The first step involved the extraction of the CBP lines from the DEM (Fig. 2). This was done as follows:

The following outlines the steps which were used for the creation of the CBPs.

(1) Delineated sub-watersheds for each DEM were generated as shown in Fig. 1. The most critical component of the watershed delineation was to ensure that all watersheds were categorised equal or above 10 km² (for 5 m resolution DEM, 10 km² = 400 000 cells). In the case of 30 m resolution ASTER DEM, the number of cells was approximated as 11 111 for the calculation.

(2) The elevation measurements at 10 m distance around the perimeter of each sub-watershed were extracted and the elevation profiles plotted against the distances. The plot of the elevation heights (m) against the distances at 10 m interval provided the CBP. The CBP were then used as input variables for the fractal dimension (FD) estimation algorithms.

(3) The FD for all the methods were compared and their applicability discussed for each of the cases.

1.4 Selection of CBP

Twentieth (12) selected CBPs were selected based on their representatives among the several profiles for representation as shown in Fig. 1. The 12 selected locations numbered from [1–12]. For the ease of presentation, SNet(*x*) denotes the *x*-th location as already shown in Fig. 1. These locations are divided into Northern and Southern Zones. For the Northern Zone (NS), the SNet(3, 4, 8, 12, 9) and the Southern Zone (SZ) represented by SNet(1, 2, 6, 7, 10).

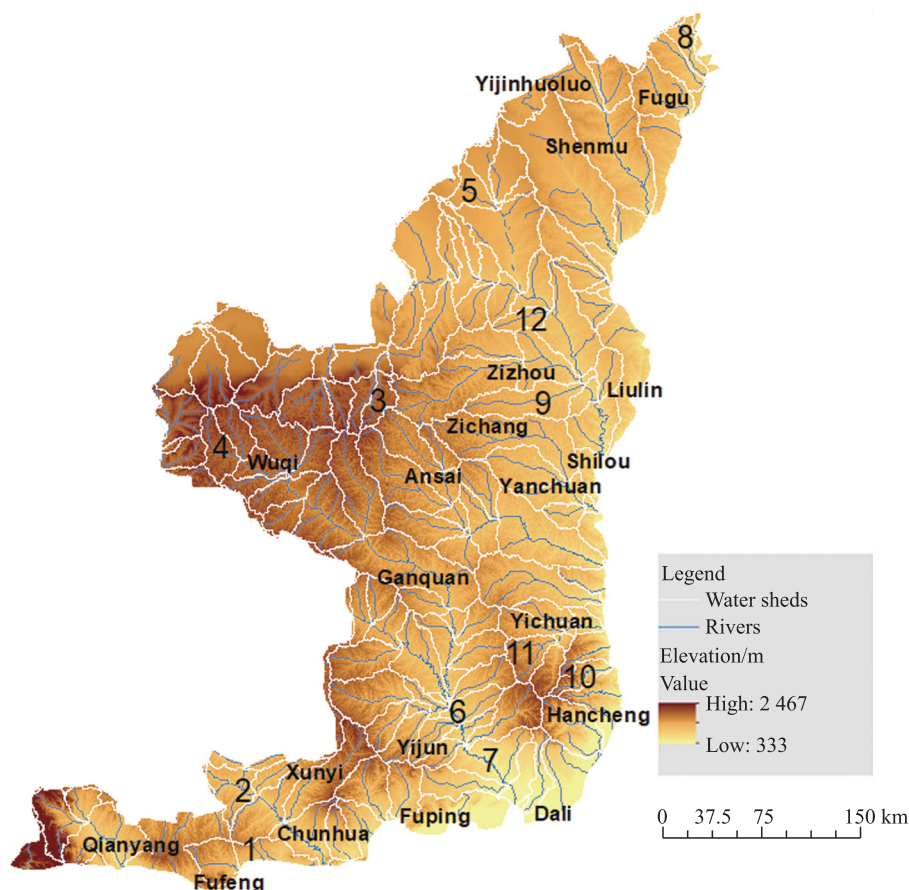


Fig. 1 The loess plateau in the Northern Shaanxi Province(The serial numbered 1–12 represent the locations of the Catchment Boundary Profile selected for the fractal analysis)

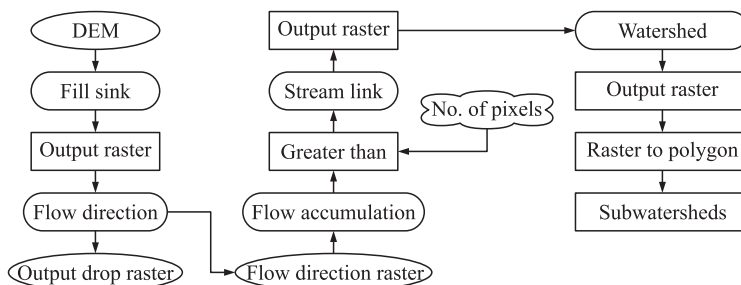


Fig. 2 Creation of sub-watersheds

1.5 Estimation fractal dimension from surface terrain

Three fractal models were applied—the Box Counting Method, the Hurst Method (HUR) and the Higuchi Method (HIG). Each of them is further described in detail below:

1.5.1 Box counting method

The BCM is sometimes call the grid or reticular cell counting method^[21]. The general mathematical form of the BCM is:

$$N(r) = Cr^{-D}, \tag{1}$$

where D is the fractal dimension, $N(r)$ is the number of boxes that cover the linear object measured, r is the side length of the square box and C is the constant. The log-log form of this equation is:

$$\log[N(r)] = -D\log(r) + \log(C). \tag{2}$$

To obtain the truthful value of D , one needs to count the $N(r)$ for different side lengths of r , then obtain the D from the data pairs $N(r)$ and r using least square regressions. This method works best for self-similar linear ob-

jects. The primary data form used with this method, is grid-based DEM.

The method has been applied to many several studies about streams, coastlines and linear features^[22]. To overcome the large computation problems associated with this method, an automated Matlab function was developed to allow for the automatic unsupervised box counting^[23].

1.5.2 Hurst exponent

The non-dimensional estimator for self-similarity of a time series is the Hurst Exponent. Harold Edwin Hurst in his definition to develop a law for regularities of the Nile water level^[24]. The Hurst Exponent H is correlated to the fractal dimension D by the relation $D=2-H$. H is an indicator to determine whether a natural phenomenon or exhibits some fractal behaviour and also measures the intensity of long term dependency of a time series^[25]. When the time series analysed is random, $H=0.5$ (white noise), persistent when $0.5<H<1$ (there is a scale invariance associated with long term positive correlations) and when $0<H<0.5$, is anti-persistent (there is a scale invariance associated with negative long-term correlations).

There are several methods for the estimation of the H parameter^[26-28]. Notwithstanding, this study made use of the rescaled range method as shown in other research as its closeness to reality^[29-30]. The rescaled range method (R/δ) proposed is based on the hydrological analysis of the Hurst^[31]. This method allows the calculation of the self-similarity parameter H , to measure the intensity of long-term dependence time series.

The Hurst Exponent can be defined in more than few approaches formally. Harold Hurst's description developed by himself as the oldest is as follows:

$$E \left[\frac{R(n)}{S(n)} \right] = Cn^H, n \rightarrow \infty. \quad (3)$$

The expected value of the rescale range is on the left hand side. $R(n)$ is defined on a time series $Y_i \{ i=1, 2, \dots, n \}$ as follows

$$R(n) = \max(Y_i, i=1, 2, \dots, n) - \min(Y_i, i=1, 2, \dots, n). \quad (4)$$

$S(n)$ is the standard deviation and C an arbitrary constant.

This produces a method instantly on how the Hurst exponent is computed.

For some $i, i=1, 2, \dots, N/5$ (where N is the length of the time series) one computes

$$a_i = E \left[\frac{R(i)}{S(i)} \right]. \quad (5)$$

For every size i , the right hand side is evaluated by partitioning the time series into mass of size i . On every mass, $R(i)$ and $S(i)$ for this specific mass computed. The expectation value $E \left[\frac{R(i)}{S(i)} \right]$ for the complete time series is then estimated by taking the average over all sub-results of all masses. This leads to the equation:

$$E[a_i] = Ci^H. \quad (6)$$

Hence,

$$\log(E[a_i]) = \log(C) + H \log(i). \quad (7)$$

With the use of more than two distinct i , these equations would be overdetermined generally on condition that there is sufficient input data and can be solved using a least squares fit. The estimated value for H becomes the slope of the fit, the constant offset the estimated value for $\log(C)$ which is insignificant in this instance. The major setback of the analyses of R/δ is the asymptotic distribution of the parameter H .

1.6 Higuchi's algorithm

The Higuchi's algorithm can be applied for the calculating fractal dimension of a time series^[32]. The power spectrum analysis has been used as an efficient and very essential method to analyze irregular time series. This is particularly true if the Power Spectrum follows the Power Law. The exponent β is the index for representing the irregularity of the time series. The use of Higuchi's fractal dimension is more appropriate than the spectral exponent β .

In order to estimate the D , Higuchi considered a finite set of observations at regular intervals

$$X(1), X(2), X(3), \dots, X(N). \tag{8}$$

From this series, a new one X_k^m is constructed, as defined below;

$$X_k^m; X(m), X(m+k), X(m+2k), \dots, X\left(m + \left[\frac{N-m}{k}\right]k\right), \tag{9}$$

where $m = 1, 2, \dots, k$; and $[\cdot]$ denotes the Gauss notation, that is the bigger integer and that both k and m are integers. m and k show that the initial and the interval time respectively.

Higuchi defines the length of the curve associated with each time series X_k^m as:

$$L_m(k) = \frac{1}{k} \left(\sum_{i=1}^{\left[\frac{N-m}{k}\right]} (X(X(m+ik)) - X(m+(i-1)k)) \right) \left(\frac{N-1}{\left[\frac{N-m}{k}\right]k} \right), \tag{10}$$

where $\frac{N-1}{\left[\frac{N-m}{k}\right]k}$ is the normalization factor. Higuchi takes the average value $\{L(k)\}$ of the lengths associated with the time series provided in the above equation.

Take for instance, if the average follows a power law, it implies that:

$$\langle L(k) \rangle \propto k^{-D}. \tag{11}$$

Then the curve is a fractal with a dimension D . Higuchi approximation can even be applied over time series not stationary. This fact shows the advantage over spectral analysis and Hurst's algorithm.

The spectral exponent β is then related to the D of the time series and with the exponent H , know as the Hausdorff measure in the following equation:

$$\beta = 2H + 1 = 5 - 2D. \tag{12}$$

Higuchi proved that if $1 \leq \beta \leq 3$, then $D = (5 - \beta)/2$. He also shows that the following limits are possible:

$$\text{if } \beta \rightarrow 0 \text{ then } D \rightarrow 2. \tag{13}$$

This corresponds to uncorrelated white noise. The second limit is:

$$\text{if } \beta \rightarrow 3 \text{ then } D \rightarrow 1. \tag{14}$$

Since the values of the fractal dimension for an index time series is in the interval $[1, 2]$, then the equations highlighted can be used for analysis.

1.7 Results and discussion

1.7.1 FD of CBP for characterising landforms

The fractal dimension (FD) represents the self-similarity of a terrain morphology^[17]. An increasing value means more terrain self-similarity. Three methods were adopted for the fractal dimension estimation. The methods included the Box Counting Method (BCM), the Hurst Method (HUR) and the Higuchi Method (HIG). For each of the watershed, all the methods were applied. The authors sought to investigate the appropriateness of the fractal methods adopted for the estimation of fractal dimension in the study area. The investigation of Grid Sizes (GSs) of 16, 32 and 64 indicated that, the GS 32 was adequate and appropriate as it provided the best results. This is because GS affect the estimation of FD and hence GS are site specific. It is very possible that in another landforms study, another grid size may be tenable. Therefore, care must always to taken to consider at least three grid size windows before a decision made on the grid size. As discussed previously, the CBP extracted for the 12 locations shown in Fig. 3 are the basis of the discussion of the results here. Table 1 provides an overview of the fractal dimension, geomorphological characteristics and the landform type for each of the locations.

Table 1 Landform properties of the 12 selected locations

Serial	FD	Landform type (P-N) ^[13]	Geomorpho- logy ^[34]	Properties		
				Vegetation cover ^[13]	Erosion modulus ^[13] /(t/(km ² ·yr))	Land use types ^[13]
1	BCM = 1.32 HUR = 1.60 HIG = 1.40	Loess ridge	Erosion and denudation-low loess mountains	Temperate typical grassland sub-zone, temperate forest-grassland sub-zone and north warm-temperate deciduous oak forest sub-zone	5 000–10 000	Mainly non-irrigated field, a little bush, timber forest and prairie grass-land Loess
2	BCM = 1.39 HUR = 1.57 HIG = 1.47	Loess incision gorge hill	Loess ridge and hill	The northern part; temperate typical grassland sub-zone; The eastern part; temperate forest-grassland sub-zone and warm-temperate deciduous oak forest sub-zone	20 000–25 000 mainly water erosion	Mainly non-irrigated field with a little prairie grass-land in parts of the northern sector
3	BCM = 1.54 HUR = 1.65 HIG = 1.65	Loess ridge hill	Loess ridge and hill	Temperate typical grassland sub-zone and temperate forest grassland subzone	5 000–10 000 Mainly water erosion	Mainly non-irrigated field, a little bush, timber and prairie grassland
4	BCM = 1.56 HUR = 1.72 HIG = 1.66	Rocky low hill	Erosion and denudation-low loess mountains	Warm temperate deciduous oak forest zone	2 000–10 000 mainly water erosion	Hill grass land, timber and forest and little non-irrigated field and bush
5	BCM = 1.44 HUR = 1.66 HIG = 1.53	Loess ridge	Loess ridge (flat ridge)	Temperate typical grassland sub-zone, temperate forest-grassland sub-zone and north warm-temperate deciduous oak forest sub-zone	5 000–10 000	Mainly non-irrigated field, a little bush, timber forest and prairie grass-land Loess
6	BCM = 1.42 HUR = 1.60 HIG = 0.00	Loess ridge hill	Loess ridge and hill	Temperate typical grassland sub-zone and temperate forest grassland subzone	5 000–10 000 mainly water erosion	Mainly non-irrigated field, a little bush, timber and prairie grassland
7	BCM = 1.34 HUR = 1.53 HIG = 1.36	Rocky low hill	Residual loess tableland	Warm temperate deciduous oak forest subzone	2 000–10 000 mainly water erosion	Non-irrigated field and irrigated field
8	BCM = 1.47 HUR = 1.69 HIG = 1.56	Rocky low hill	Residual loess tableland	Warm temperate deciduous oak forest subzone	2 000–10 000 mainly water erosion	Non-irrigated field and irrigated field
9	BCM = 1.51 HUR = 1.72 HIG = 0.00	Loess low hill	Erosion and denudation-low loess mountains	Temperate typical grassland subzone	5 300–8 000 mainly wind erosion	Mainly prairie grassland, a little desert and non-irrigated field
10	BCM = 1.36 HUR = 1.57 HIG = 1.37	Loess low hill	Loess ridge (long ridge)	Temperate typical grassland subzone	5 300–8 000 mainly wind erosion	Mainly prairie grassland, a little desert and non-irrigated field
11	BCM = 1.27 HUR = 1.49 HIG = 1.36	Desert loess transitional area	Loess ridge and hill	Temperate semi-desert grassland subzone	4 000–6 700 mainly wind erosion	Mainly desert, a little non-irrigated field
12	BCM = 1.48 HUR = 1.72 HIG = 1.60	Loess tableland	Loess plain tableland	Warm temperate deciduous oak forest subzone	2 000–5 000 mainly water erosion	Non-irrigated field, bush and little irrigated field

SNet(7) is located in the low loess mountainous area with typical temperate grassland, some forests grassland and deciduous oak forest zone as indicated in previous works of Zhou et al^[33]. The area is also depicted by mainly non-irrigated agriculture practices with little bushes of grass and timber forest. Recent research from Zhou et al^[33] shows that the erosion in this area is typically estimated around 5 000–10 000 t/(km²·yr). This confirms with a relatively high fractal values obtained by the different methods (BCM = 1.34; HUR = 1.53; HIG = 1.36) as shown in Fig. 3(g). There is consistent between the values obtained from the BCM and HIG. The inconsistency of the HUR could be attributed to its sensitivity of the estimation of the exponent coefficient, *H*. The values showed

that there is considerable amount of anthropogenic activity in the selected zone, which can be attributed to the agricultural activities indicated by Zhou et al. (2010) studies. From SNet(7), there are also signs of bifurcation as a result of the erosion. This is indicated by the peaking and valleys of the CBP graph.

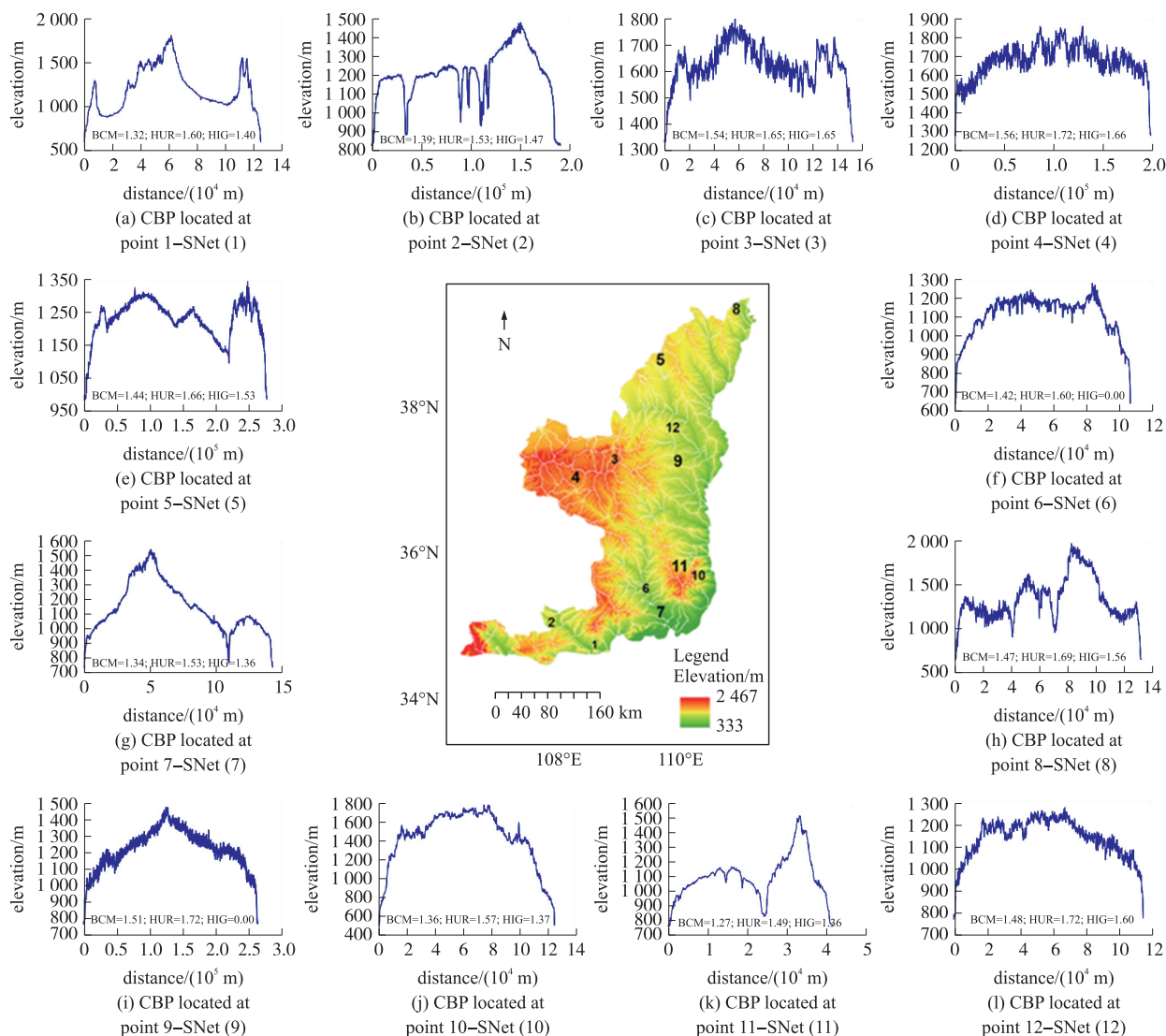


Fig. 3 CBPs for 12 selected locations across the study area

Research from Zhou et al.^[33] shows that SNet(8) experiences mainly water erosion spanning from 20 000 $t/(km^2 \cdot yr)$ to 25 000 $t/(km^2 \cdot yr)$. The graph (Fig. 3(h)) shows three peaks with deep depression possibly as cause of bifurcation activities resulting from the massive erosion. This location is the farthest part of the study area and shows FD values as [BCM = 1.47; HUR = 1.69; HIG = 1.56]. The different methods show variation in the estimates with slight differences between BCM and HIG. The location represents the landform types-Loess Ridge and Hill. The large values of the CBP could be attributed to the agricultural activities in the area usually using non-irrigated field methods. It is also very similar to the SNet(7) in that, this is also characterised by temperate grassland and forest. However, the FD values for the SNet(8), are slightly larger than that of the SNet(7). This could be attributed to the different degrees of erosion in both locations. For instance, SNet(8)'s FD values are almost twice that of the SNet(7). This implies, SNet(8) could experience higher degree of erosion, compared to SNet(7).

SNet(9) shows a symmetrical loess ridge hill (See Fig. 3(i)). The FD values are in the ranges [BCM = 1.51; HUR = 1.72; HIG = 0.00]. The values for the different methods show some variation with the HIG failing completely. The location is characterised by erosion in the amounts of 5 000–10 000 $t/(km^2 \cdot yr)$, much lesser

than SNet(8), and comparable to SNet(7), with similar anthropogenic activities e.g. non-irrigated agricultural practices and the support of timber industries.

SNet(11) as in Fig. 3(k) shows a two-peak profile of loess ridges with the possibility of bifurcation through erosion. The climate and the anthropogenic activities are similar to that of SNet(7). However, the FD values are different [BCM = 1.27; HUR = 1.49; HIG = 1.36]. The FD values show that the erosion potentials are slightly lesser than SNet(7). SNet(12) has FD values ranging from [BCM = 1.48; HUR = 1.72; HIG = 1.60] (Fig. 3(l)) and show similarities to SNet(9). It is symmetrical and show similar conditions as in SNet(9) in terms of the agriculture practices and erosion occurrence.

SNet(1) and SNet(2) show relatively moderate erosion estimates from 2 000–10 000 t/(km²·yr) as a result of water erosion. Respectively the FD values for SNet(1) and SNet(2) respectively in Fig. 3(a) and Fig. 3(b) show that [BCM = 1.32; HUR = 1.60; HIG = 1.40] and [BCM = 1.39; HUR = 1.53; HIG = 1.47]. SNet(1) shows three peaks at elevations of 1 250 m, 1 600 m and 1 750 m but generally smoothed out in terms of profile compared to SNet(2). SNet(2) shows five(5) distinct signs of possible bifurcation in the watershed. Zhou et al^[33] estimated for the rocky low hill to be in the range of 2 000–10 000 t/(km²·yr), it is evident from the fractal values that, the SNet(2) shows higher erosion potential compared to SNet(1). In this case, the SNet(2) can be assumed to have erosion values nearer to 10 000 t/(km²·yr) compared to SNet(1). More intense bifurcation in the watersheds indicate the high level of erosion over a long geological period, and meaning, more complex terrain surfaces formed at the end of this period. Both SNet(1 and 2) represent locations with warm temperate deciduous oak and forest zone in both cases. Man-made activities primarily agriculture practised is both rain-fed agriculture and irrigation.

The SNet(3) and SNet(4) as in Fig. 3(c) and 3(d) have similar profile as shown in the figure above. The profile indicates a rapid changing terrain surface within either of the watersheds. The FD values obtained for SNet(3) and SNet(4) show [BCM = 1.54; HUR = 1.65; HIG = 1.65] and [BCM = 1.56; HUR = 1.72; HIG = 1.66] respectively. The SNet(4) shows slightly higher values of FD compared to SNet(3). This could be attributed to more anthropogenic (agriculture and forestry) activities compared to SNet(3). In reference to the geomorphological features, both sites represent the loess low hill characterised by erosion and denudation coupled with long ridges. The estimated wind erosion in these watersheds is around 5 300–8 000 t/(km²·yr). The agricultural practises are mainly non-irrigated methods-but it is saddled with pastures of prairie grassland and little desert. SNet(5) shows desert loess transitional area with loess ridges and hills. The location is eroded by wind with estimated amounts of 4 000–6 700 t/(km²·yr). The FD for the location ranges [BCM = 1.44, HUR = 1.66; HIG = 1.53] as in Fig. 3(e). The BCM and HIG methods agree perfectly in estimation of FD.

The SNet(6) represents the typical loess tableland; relatively warm temperate with water erosion amounting to about 2 000–5 000 t/(km²·yr). The FD values ranges [BCM = 1.42, HUR = 1.60, and HIG = -0.0] as in Fig. 3(f). Agricultural practices here are rain-fed and some degree of irrigation.

1.7.2 FD methods applicability

Three methods of fractal estimation for profile lines were investigated in the study. They are the widely used technique—BCM, HUR and HIG. The fractal dimension estimation clearly provided a way of characterizing the geomorphological features in each watershed. The FD showed a direct relationship with the CBP, clearly showing that the fractal theory can be reliably applied for the characterizing the watershed's geomorphological complexity. However, there were some differences in the methods for their representativeness to reality in their estimation. A comparison of the methods is shown below in Table 2.

Table 2 Comparison and applicability of the three fractal estimation methods

Method	Consistency & Reality	Estimation Errors	Remarks
BCM	Yes	No	<ul style="list-style-type: none"> • The estimation of all sub-watersheds were consistent. • There was no estimation errors in the determination of the FD for each sub-watershed. • The method reliably was able to characterize the hypsometric profiles for each watershed. • FD values obtained were close to reality. • It confirms the reasons for the wide-used of the box counting method.
HUR	No	No	<ul style="list-style-type: none"> • The FD estimates were not consistent and generally deviated largely when compared with BCM and the HIG. • This implies the Hurst Exponent is sensitive as depicted in other researches.
HIG	Yes	Yes	<ul style="list-style-type: none"> • The estimation of all sub-watersheds were consistent. • The estimation for some cases failed. This is because the Higuchi algorithm finds the fractal dimension as the slope of the line of best fit between the logarithms of two parameters. When the parameters are such that the line of best fit (the describing polynomial) is not unique, it becomes impossible to obtain the FD.

1.7.3 Elevation effect

As proven in earlier discussion in the paper, results from the BCM are more reliable compared to the HIG and HUR. Thus, the BCM was used as the means of evaluation for the impact of the elevation heights and CBP on the FD values.

The SNet(7) shows a graph at a distance of 0 m at an elevation of 750 m, rises to a peak of about 1 550 m at a distance of 50 000 m along the watershed. It then drops significantly to 750 m and then rise again to 1 000 m elevation, then creates a symmetrical profile. This SNet has a two distinct peaks. The fractal value of the CBP based on the BCM is 1.34. The next SNet(8) starts at 0 m with an elevation of 800 m and rise to 1 080 m, then falls significantly to a 950, at a distance of 22 000 m, rise again to about 1 050, at a distance of 40 000 m. It repeats a similar profile in the next 40 000 m but with a higher peaking elevation of 1 150 m. At a distance of 80 000 m along the watershed, it rises to 1 250 m, then descends gradually to a halt at 850 m. This SNet has a BCM fractal value of 1.47 and has three distinct peaks. SNet(7) has higher FD values compared to SNet(8). The possible reason for the higher values for SNet(8) compared to SNet(7) could be the result of more peaking of the terrain surface in SNet(8) than SNet(7). Though, SNet(7) also has a tendency for single notifiable bifurcation in the watershed, this effect is not strong enough to have increased the FD. Hence, the large elevation effect from SNet(8) strongly influenced the FD values compared to SNet(7).

The SNet(9) starts at 0 m distance with an elevation of 800 m and rises to 1.25×10^5 m, then creates mirror at distance of 2.75×10^5 m. It has one distinct peak and resembles a normal distribution function. However, it shows slightly intense harmonic effect in its profile series. Its FD is 1.51. The FD of SNet(9) is far higher than that of the SNet(8), SNet(7) as a result of the possible distinctive four(4) peaks and harmonic effect compared to the SNet(8) and SNet(7). This harmonic effect is a result of the undulating terrain properties, hence rapid changing elevation has an influenced on raising the FD value.

The SNet(10) starts at 0 m at an elevation of 500 m through the gradual step-wise increment at a distance of 2×10^4 m to an elevation of 1 500 m. It drops gradually and rise again at a distance of 3×10^4 m to an elevation of 1 700 m, and nearly mirrors itself. The behaviour of SNet(10) is similar to SNet(9). However, SNet(10) has a FD of 1.36 compared to the 1.51 of SNet(9)^[3]. This can also be attributed to the intense harmonic and peaking effect indicated in SNet(9). Subsequently, this explains the elevation effect on FD values. High harmonic and peaking effect in the elevation results in high FD.

The SNet(11) starts a 0 m distance with an elevation of 750 m and then rise to an elevation of 1 150 m at a distance of 1.25×10^4 m, then mirrors itself with some regular peaks, and dips to a distance of 2.5×10^4 m with an elevation of 800 m. It then rise again with a gradual step-wise to a height of 1 500 m, then gradually drops to height of 750 m at a distance of 4.25×10^4 m. It generally shows two distinct peaks with a FD of 1.27. Its profile is

similar to SNet(7) and SNet(10). However, the stronger harmonic effect in the profiles and peaking of SNet(7) and SNet(8), give them a much higher FD compared to SNet(11). SNet(12) is similar to SNet(9) except that it starts an elevation of 800 m at the 0 m point, rises to 1 400 m through a step-wise increments to a distance of 0.75×10^5 m; drops at a distance of 1.25×10^5 m, then rises again at 1.4×10^5 m, drops finally at 800 m at a 1.8×10^5 m distance. The harmonic effect in SNet(12) and peaking compared to SNet(9) is lesser, and hence has a smaller FD of 1.46.

The SNet(1) is similar to SNet(7) and SNet(11). It starts at an elevation of 550 m at a 0 m distance and rises steeply to 1 250 m, then drops at 1×10^4 m, then rises gradually through a number of distinct steps to 1 800 m and through a smooth profile to an elevation of 1 200 m at 10×10^4 m. It then rise 1 500 m at 11×10^4 m; then drops finally at 550 m. The FD values for the SNet(1) is 1.32. The SNet(7) is higher than SNet(1) but also higher than SNet(11). With reference to SNet(7) and SNet(1), the possible difference is as a result of the bifurcation. For instance, SNet(1) has three peaks in comparison to two distinct peaks of SNet(11). Therefore, SNet(1) has a higher FD compared to SNet(11). This case also showcase the considerable effect of elevation rapid changes with increase of FD.

The SNet(2) is similar to SNet(11), SNet(1) and SNet(7). Its graph starts at 0 m point with an elevation of 1 200 m then gradually descends to 900 m at a distance of 0.4×10^5 m. It rises again to 1 200 m and gradually, at a distance of 0.75×10^5 m rises to 1 250 m. It drops for this distance to 950 m height and rises back to 1 200 m at a distance of 1×10^5 m. It creates a mirror. At this mirror, it rises at a distance of 1.5×10^5 m to a peak elevation of 1 500 m, gradually descends to 850 m at 1.8×10^5 m. SNet(2) has six(6) distinct peaks and obviously has higher FD of 1.39 compared to similar watersheds' profile such as SNet(1) and SNet(11). In addition, the bifurcation effect is additional factor for the increase in the FD compared to the others. Rapid changing elevation coupled with the bifurcation effect can give rise to higher FD, as explained here.

SNet(3) starts at 1 320 m at 0 m point distance, and rise to 1 700 m at a 1×10^4 m distance. It then drops to 1 500 m at a distance of 2.5×10^4 m. It rises through step-wise increments to a height of 1 800 m at a distance of 6×10^4 m. It descends through a dense-reduced to a height of 1 550 m at a distance of 12×10^4 m. It rises for this stance to a height of 1 700 m through short and fall to low height of 1 570 m at a distance of 14×10^4 m, then mirrors itself. This profile has four(4) distinct peaks with a FD of 1.54. SNet(3) is closer in similarity to [3], but due to its more peaks, has higher FD compared to the SNet(9) with an FD of 1.51.

SNet(4) shows similarities with SNet(9) and SNet(3). It starts at 0 m with an elevation of 1 280 m and then rises step-wise through several harmonic effects to a height of 1 750 m at a distance of 0.8×10^5 m, it drops to 1 550 m and again, rises to 1 850 m at a distance of 0.8×10^5 m. At this point, it creates a mirror. This mirror is repeated roughly three times then at a distance of 1.5×10^5 m rises to 1 700 m then descends to a height of 1 280 m. At a distance of 1×10^5 m, then graph is symmetrical with four(4) distinct peaks to the right and left. SNet(4) has in total eight(8) distinct peaks and has a FD of 1.56 and hence is much higher compared to SNets(3, 9, 12).

The SNet(5) is similar in profile characteristics to SNets(3, 7, 8, 11) but however with an intense profile harmonics compared to the others. This SNet starts at an elevation of 980 m rises gradually to 1 330 m at a distance of 0.8×10^5 m and then drops at a gentle slope to a low height of 1 100 m, then rises step-wise to a height of 1 350 m at a distance of 1.5×10^5 m then drop finally at 980 m elevation. The FD value for SNet(5) is 1.44. SNet(3) has more peaks than SNet(5), hence has a higher fractal value. Also, SNet(5) has more peaks and more harmonic effect and hence have higher FD values compared to SNet(2). This result is comparable for SNets(5, 11, 7). SNet(8) has more peaks, and hence has a higher FD compared to SNet(5). A look at SNet(6) show close profile characteristics with SNets(12, 9, 10). It starts with an elevation of 550 m at 0 m distance, rises to 1 200 m with a step-wise increment, rise and fall through a 100 m depth, and then drops at a distance of 8×10^4 m with a height of 1 100 m. It then rises to 1 250 m then drops finally at to low height of 550 m. SNet(12) and SNet(9) has more peaks and possible harmonic effect, and hence has higher FD values compared to SNet(6) with an FD

value of 1.42. However, SNet(10) also has lesser FD value compared to SNet(6) with the same result of peaking and harmonic effect.

In general, the peaking and the harmonics effects of the CBP series indicate the degree of complexity of the terrain, the more complex and intense a CBP is; the higher the fractal dimension. This has been strongly demonstrated in this research that peaking and harmonic effect have a direct correlation with the FD behaviour. Also, peaking and the harmonic effect, show the degree and potential of erosion activity in the watershed. Therefore, the ability of FD to reflect this property is key to understanding the phenomenal behaviour of watersheds using CBP approach.

1.7.4 Bifurcation effect on the CBP

There are visible of some possible bifurcation effects in a number of the CBPs as shown in SNet(2, 7, 8 and 11). For instance, for SNet(2) shows possible bifurcation effects at locations 1×10^4 m, 6×10^4 m, 9×10^4 m and 14.5×10^4 m with V-shaped valleys (saddle bifurcation) at distances of 4.5×10^4 m, 7×10^4 m and 8×10^4 m. The FD for SNet(2) is 1.39. In the case of SNet(7) the bifurcation effect is identified at distances of 0.5×10^4 m, 5×10^4 m and 12.5×10^4 m. There is also bifurcation effects in the form of saddles at a distance of 11×10^4 m. The FD for SNet(7) is 1.34. At distances of 0.25×10^5 m, 0.75×10^5 m, 0.9×10^5 m, 1×10^5 m, 1.25×10^5 m, 1.5×10^5 m with V-shaped valleys at distances of 0.3×10^5 m, 0.8×10^5 m, 1×10^5 m, 1.1×10^5 m and 1.2×10^5 m. The FD for SNet(8) is 1.47. Bifurcation effects have also been identified in SNet(11) at distances of 1.25×10^4 m, 1.75×10^4 m and 3.5×10^4 m with a V-shaped valley at distance of 2.5×10^4 m. The FD for SNet(11) is 1.27.

The above findings show that the higher the number of bifurcation effects within the terrain, the higher the possible estimate for the FD. For instance, SNet(8) has a higher FD compared to SNet(2), SNet(8) and SNet(11) as a result of the higher bifurcation effects on the terrain. V-shaped valleys are generally formed a result of water erosion in the terrain. Aside this, the findings also show that CBP could provide some insights to bifurcation effects in a landform.

The above findings also indicate that the bifurcation result in harmonic effect within the watershed, which results in severe erosion and that leads to the increment in fractal values. It is recommended that future studies may consider the establishment of mathematical relationships between the fractal value and the bifurcation ratio as this was not part of this current research under consideration.

2 Conclusion

Deeper analysis of the fractals for the CBP is necessary to interpret the landform complexities and dynamics. In this paper, the authors assessed the fractal dimension of CBP in order to characterize the geomorphological features of small watersheds in the Northern Shaanxi Province of China. Three methods were used—(1) BCM, (2) HUR and (3) HIG. The first method was able to reliably estimate the fractal dimension in all cases without any fail, the second method—Hurst exponent in most cases over-estimated the fractal dimension while the last method results were similar to that of the box counting method. The results also demonstrated that peaking and harmonic effect of the CBP profile have a direct correlation to the fractal values obtained. The results from the fractal dimension and CBPs show a close link with the various landform types—loess hill, loess low hill, loess rocky low hills and loess tableland and their phases of anthropogenic and geomorphic activity. Therefore, the fractal methodology is applicable for the characterizing the geomorphic features of the loess plateau under study. The paper hopes to provide a detailed baseline information for fractal studies in the Loess Plateau and to complement future studies in the case of land use planning in this region.

Acknowledgment

We wish to acknowledge all anonymous reviewers including School of Geography of Nanjing Normal University, China for the support to carry out this research. The authors also thank Mr. David Oppong for his thorough

review of the Programming Codes on MatLab; and support from University of Energy and Natural Resources, Ghana.

References

- [1] LÜ G, XIONG L, CHEN M, et al. Chinese progress in geomorphometry [J]. *Journal of geographical sciences*, 2017, 27(11) : 1389–1412.
- [2] AN Z, KUKLA G J, PORTER S C, et al. Magnetic susceptibility evidence of monsoon variation on the Loess Plateau of central China during the last 130 000 years [J]. *Quaternary research*, 1991, 36(1) : 29–36.
- [3] FU B, CHEN L, MA K, et al. The relationships between land use and soil conditions in the hilly area of the loess plateau in northern Shaanxi, China [J]. *Catena*, 2000, 39(1) : 69–78.
- [4] ZHAO T, YANG M, WALLING D E, et al. Using check dam deposits to investigate recent changes in sediment yield in the Loess Plateau, China [J]. *Global and planetary change*, 2017, 152 : 88–98.
- [5] ZHAO G, KONDOLF G M, MU X, et al. Sediment yield reduction associated with land use changes and check dams in a catchment of the Loess Plateau, China [J]. *Catena*, 2017, 148(2) : 126–137.
- [6] GUOAN T, MUDAN Z, TIANWEN L, et al. Simulation on slope uncertainty derived from DEMs at different resolution levels; a case study in the Loess Plateau [J]. *Journal of geographical sciences*, 2003, 13(4) : 387–394.
- [7] XIONG L, TANG G, YAN S, et al. Landform-oriented flow-routing algorithm for the dual-structure loess terrain based on digital elevation models [J]. *Hydrological process*, 2014, 28(4) : 1756–1766.
- [8] TANG G, JIA Y, YANG X, et al. The profile spectrum of catchment boundary basing on DEMs in loess plateau [C] // the 24th international cartographic conference. Santiago, Chile, 2009 : 15–21.
- [9] TANG G, LI F, LIU X, et al. Research on the slope spectrum of the Loess Plateau [J]. *Science in China series E: technological sciences*, 2008, 51(1) : 175–185.
- [10] HESSEL R, VAN ASCH T. Modelling gully erosion for a small catchment on the Chinese Loess Plateau [J]. *Catena*, 2003, 54(1/2) : 131–146.
- [11] ZHANG H Y, SHI Z H, FANG N F, et al. Linking watershed geomorphic characteristics to sediment yield: evidence from the Loess Plateau of China [J]. *Geomorphology*, 2015, 234 : 19–27.
- [12] CHENG N N, HE H M, YANG S Y, et al. Impacts of topography on sediment discharge in Loess Plateau, China [J]. *Quaternary international*, 2017, 440 : 119–129.
- [13] Zhou Y, Tang G, Yang X, et al. Positive and negative terrains on northern Shaanxi Loess Plateau [J]. *Journal of geographical sciences*, 2010, 20(1) : 64–76.
- [14] TURCOTTE D L. *Fractals and chaos in geology and geophysics* [M]. Cambridge: Cambridge University Press, 1997 : 412.
- [15] ZHOU B, WANG J, WANG H. Three-dimensional sphericity, roundness and fractal dimension of sand particles [J]. *Geotechnique*, 2017, 68(1) : 18–30.
- [16] PESQUET P B, VÉHEL J L. Stochastic fractal models for image processing [J]. *IEEE signal processing magazine*, 2002, 19(5) : 48–62.
- [17] LI M, YANG X, NA J, et al. Regional topographic classification in the North Shaanxi Loess Plateau based on catchment boundary profiles [J]. *Progress in physical geography*, 2017, 41(3) : 302–324.
- [18] WANG X, JIAO F, LI X, et al. The loess plateau [M] // Multifunctional land-use systems for managing the nexus of environmental resources. Cham: Springer, 2017 : 11–27.
- [19] USGS. Earth explorer [J / OL]. [2019-03-01]. <https://earthexplorer.usgs.gov/>.
- [20] TACHIKAWA T, KAKU M, IWASAKI A, et al. ASTER global digital elevation model version 2-summary of validation results [R]. Washington D.C. : NASA, 2011.
- [21] KLINKENBERG B. A review of methods used to determine the fractal dimension of linear features [J]. *Mathematical geology*, 1994, 26(1) : 23–46.
- [22] RODRIGUEZ I, RINALDO A I. *Fractal river basins: chance and self-organization* [M]. Cambridge: Cambridge University Press, 2001 : 564.
- [23] ANGELES G R, PERILLO G M E, PICCOLO M C, et al. Fractal analysis of tidal channels in the Bahía Blanca Estuary (Argentina) [J]. *Geomorphology*, 2004, 57(3/4) : 263–274.

- [24] ZHAO X, WANG X. Fractal dimension estimation of Rgb color images using maximum color distance[J]. *Fractals*, 2016, 24(4):1650040.
- [25] ORTIZ J P, AGUILERA R C, BALANKIN A S, et al. Seismic activity seen through evolution of the hurst exponent model in 3D[J]. *Fractals*, 2016, 24(4):1650045.
- [26] MIELNICZUK J, WOJDYŁO P. Estimation of Hurst exponent revisited[J]. *Computational statistics & data analysis*, 2007, 51(9):4510–4525.
- [27] ZHANG H F, SHU Y T, YANG O. Estimation of Hurst parameter by variance-time plots[C]//1997 IEEE Pacific Rim Conference on Communications, Computers and Signal Processing, PACRIM. 10 Years Networking the Pacific Rim, 1987–1997. Victoria B.C.:IEEE, 1997:883–886.
- [28] VAZIRI G, ALMASGANJ F, JENABI M S. On the fractal self-similarity of laryngeal pathologies detection; the estimation of Hurst parameter[C]//2008 International Conference on Information Technology and Applications in Biomedicine. Shenzhen: IEEE, 2008:383–386.
- [29] GILMORE M, YU C X, RHODES T L, et al. Investigation of rescaled range analysis, the Hurst exponent, and long-time correlations in plasma turbulence[J]. *Physics of plasmas*, 2002, 9(4):1312–1317.
- [30] BASSINGTHWAIGHTE J B, RAYMOND G M. Evaluating rescaled range analysis for time series[J]. *Annals of biomedical engineering*, 1994, 22(4):432–444.
- [31] SAKALAUSKIEN G. The hurst phenomenon in hydrology[J]. *Environmental research, engineering and management*, 2003, 3(25):16–20.
- [32] CERVANTES-DE LA TORRE F, GONZÁLEZ-TREJO J I, REAL-PAMIREZ C A, et al. Fractal dimension algorithms and their application to time series associated with natural phenomena[C]//Journal of Physics: Conferences Series. IOP Publishing, 2013, 475. doi:10.1088/1742-6596/475/1/012002.
- [33] ZHOU Y, TANG G, YANG X, et al. Positive and negative terrains on northern Shaanxi Loess Plateau[J]. *Journal of geographical sciences*, 2010, 20(1):64–76.
- [34] Editorial Board of the People's Republic of China Landform Atlas. *Geomorphological Atlas of the People's Republic of China (1:1 000 000)*[M]. Beijing: Science Press, 2009:125–128.

[责任编辑: 丁 蓉]